

Energy & Environmental Science

Accepted Manuscript



This is an *Accepted Manuscript*, which has been through the Royal Society of Chemistry peer review process and has been accepted for publication.

Accepted Manuscripts are published online shortly after acceptance, before technical editing, formatting and proof reading. Using this free service, authors can make their results available to the community, in citable form, before we publish the edited article. We will replace this *Accepted Manuscript* with the edited and formatted *Advance Article* as soon as it is available.

You can find more information about *Accepted Manuscripts* in the [Information for Authors](#).

Please note that technical editing may introduce minor changes to the text and/or graphics, which may alter content. The journal's standard [Terms & Conditions](#) and the [Ethical guidelines](#) still apply. In no event shall the Royal Society of Chemistry be held responsible for any errors or omissions in this *Accepted Manuscript* or any consequences arising from the use of any information it contains.

ARTICLE

Sub 150 °C Processed Meso-superstructured Perovskite Solar Cells with Enhanced Efficiency

Cite this: DOI:
10.1039/x0xx00000x

Konrad Wojciechowski, Michael Saliba, Tomas Leijtens, Antonio Abate and Henry J. Snaith*

Received 00th January 2012,
Accepted 00th January 2012

DOI: 10.1039/x0xx00000x

www.rsc.org/

The ability to process amorphous or polycrystalline solar cells at low temperature (<150 °C) opens many possibilities for substrate choice and monolithic multijunction solar cell fabrication. Organometal trihalide perovskite solar cells have evolved rapidly over the last two years, and the $\text{CH}_3\text{NH}_3\text{PbX}_3$ (X= Cl, I or Br) material is processed at low temperature. However the first embodiments of the solar cell were composed of high temperature processed (500 °C) compact and mesoporous layers of TiO_2 . The sintering of the mesoporous TiO_2 has been negated by replacing this with a mesoporous insulating scaffold in the meso-superstructured solar cell (MSSC), yet the high temperature processed compact TiO_2 layer still persists in the most efficient devices. Here we have realised a low temperature route to compact TiO_2 , tailored for perovskite MSSC operation. With our optimized formulation we demonstrate full sun solar power conversion efficiencies of up to 15.9 % in an all low temperature processed solar cell.

1. Introduction

Lightweight and mechanically flexible photovoltaic devices are of an increasing interest and demand, mainly due to their ease of integration and versatile functionality. Potential applications range from portable electronic devices, electronic textiles, synthetic skin, robotics, aerospace technology to large scale industrial roofing¹⁻⁵. Commercially attractive reel-to-reel processing is contingent on low temperature technology in order to fabricate devices on the cheapest deformable flexible substrates, such as polyethylene terephthalate (PET) and polyethylene naphthalate (PFN). Additionally, low temperature fabrication allows for the possibility of new multijunction device architectures, as has been a successful route to higher efficiencies for organic photovoltaics⁶, and the highest efficiency crystalline photovoltaic technologies⁷. A recently emerged class of solution-processed hybrid solar cells are based on organometal trihalide perovskite absorbers, which exhibit exceptional performance⁸⁻¹¹ and are already approaching the performances of the best thin film technologies^{12,13}. This cell type

has been shown to work without high temperature sintering steps for the mesoporous scaffold¹¹, closing the gap to achieving fully low-temperature solution-based manufacture. There have recently been a few reports of low temperature processed perovskite solar cells employing all organic p and n-type contacts¹⁴⁻¹⁶. However, for both the planar heterojunction and mesosuperstructured solar cells, the highest efficiency devices still require sintering of the TiO_2 compact layer, working as a selective contact for electron collection at the anode¹⁷. Typically, this compact layer is prepared by spin-coating or spray pyrolysis of a solution of TiO_2 precursor with subsequent sintering at 500 °C in order to transform the amorphous oxide layer into the crystalline form (anatase), which provides good charge transport properties. The problem of high temperature processing of the TiO_2 compact layer has been addressed previously for dye-sensitized solar cells (DSSCs): atomic layer deposition^{18,19}, microwave sintering²⁰ and inductively coupled plasma (ICP)-assisted DC magnetron sputtering²¹ have been used for deposition. However, the results generally yield lower efficiency in DSSCs than high-

temperature processed TiO₂. Here we report a low temperature fabrication (<150 °C) of a compact layer composed of highly crystalline small nanoparticles of anatase TiO₂ (diameter < 5nm) dispersed in an alcoholic solvent with an addition of titanium diisopropoxide bis(acetylacetonate) (TiAcAc). This approach results in a dense TiO₂ layer with up to 100 fold higher conductivity than the TiO₂ produced from the previous high temperature route. The ensuing all-low-temperature processed MSSC outperform the previous state-of-the-art devices, delivering a maximum full sun power conversion efficiency of 15.9 %.

2. Results and Discussion

In this work, we compare the newly developed TiO₂ compact layer, which we term low temperature TiO₂ (lt-TiO₂), with the standard recipe used in MSSCs in which a solution of titanium isopropoxide in acidic ethanol is spin-coated upon the substrate¹¹. For the conventional route, we either dry the films at 150 °C (which we term amorphous TiO_x) or we sinter the films at 500 °C as is done in the current state-of-the-art (which we term high temperature (ht)-TiO₂). Here, we synthesize TiO₂ nanoparticles by a nonaqueous route from titanium tetrachloride and benzyl alcohol²², the detailed procedure is described in an experimental section. In Figure 1c we show the X-ray diffraction (XRD) spectrum of a powdered sample, which can be assigned to anatase TiO₂ with a crystal diameter of approximately 4.5 nm, as determined by Scherrer peak width analysis²³.

Elsewhere, we have shown that adding TiAcAc to TiO₂ mesoporous single crystals can greatly enhance the adhesive properties of the film and enhance the operation of dye-sensitized solar cells when processed at low temperature²⁴. Here, we added a small amount of TiAcAc (initially 10 mol % with respect to TiO₂ content) to the colloidal TiO₂ dispersion, prior to spin-coating and drying at 150 °C. We propose that the TiAcAc decomposes to TiO_x during film drying,

and bridges the gaps between the nanoparticles, otherwise put it creates the mortar to hold the nanoparticles together²⁵. We note that we observed that an opaque dispersion of TiO₂, becomes translucent a few hours after TiAcAc addition, which we attribute this to the chelation of acetylacetonate ligands to the TiO₂ nanoparticles²⁶. We show SEM images of the spin-coated lt-TiO₂ films in Figure 1a-b and S1a-c, which exhibit “crack free” uniform continuous coverage of the substrates.

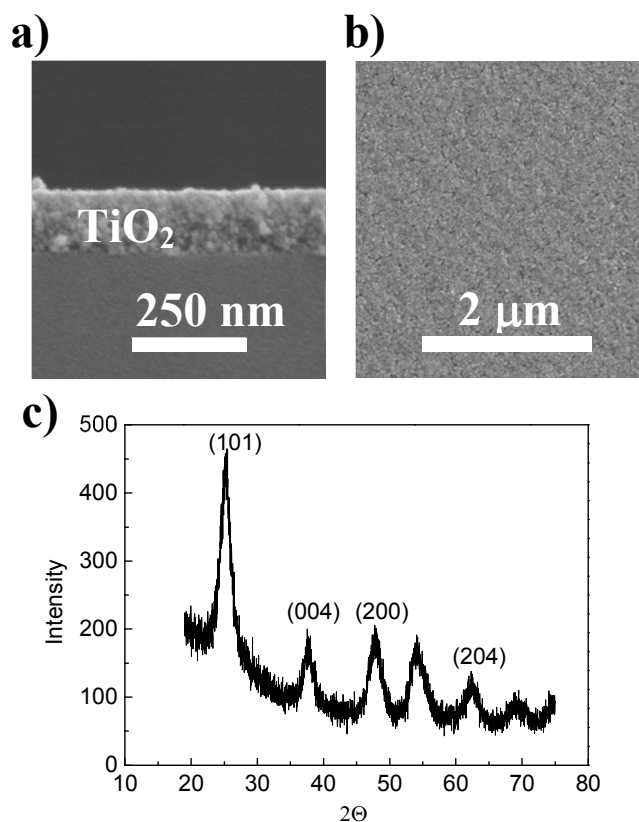


Figure 1. (a) Cross-sectional image of 3.54 weight% TiO₂ NPs spin-coated on glass, thickness: 100-120 nm; (b) top surface image of lt-TiO₂; (c) X-ray diffraction spectrum of TiO₂ nanoparticles powder sample.

We investigated the impact of varying the concentration of TiAcAc from a 0 to 80 mol % with respect to TiO₂ upon the conductivity of the films, and compared them to the standard fabricated TiO₂ films. The results that we show in Table 1 demonstrate that TiO_x is the least conductive ($2 \times 10^{-6} \text{ Scm}^{-1}$), an order of magnitude lower than the conventional ht-TiO₂. Remarkably, even the TiO₂ sol shows 50-

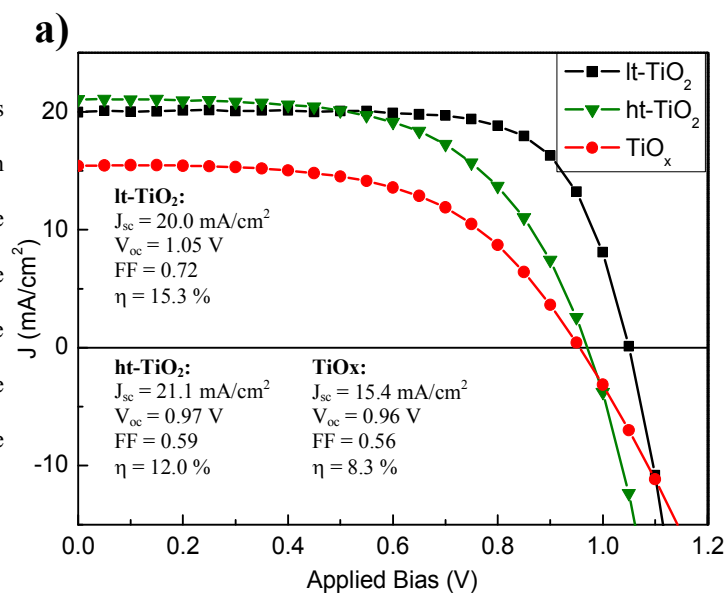
fold increase in conductivity over the ht-TiO₂ and with the addition of a small amount of TiAcAc this increases to maximum of just below 10⁻³ Scm⁻¹. This demonstrates that at least as far as conductivity and hence series resistance are concerned, the new low temperature TiO₂ compact layer should be better than the previous state-of-the-art. However, if we calculate the equivalent series resistance for current flowing perpendicularly through a 1 cm² slab of 50 nm thick material, as we also show in Table 1, only the TiO_x should contribute significantly to the solar cells series resistance.

Table 1. Conductivity values of different blocking layers.

Blocking layer	Conductivity (Scm ⁻¹)	Calculated
		Resistance through 50 nm thick film (Ωcm ²)
TiO _x	0.02·10 ⁻⁴	2.500
ht-TiO ₂	0.11·10 ⁻⁴	0.455
lt-TiO ₂ (0 mol% TiAcAc)	5.08·10 ⁻⁴	0.010
lt-TiO ₂ (10 mol% TiAcAc)	8.32·10 ⁻⁴	0.006
lt-TiO ₂ (20 mol% TiAcAc)	6.80·10 ⁻⁴	0.007
lt-TiO ₂ (40 mol% TiAcAc)	4.15·10 ⁻⁴	0.012
lt-TiO ₂ (80 mol% TiAcAc)	0.24·10 ⁻⁴	0.208
spiro-OMeTAD (250 nm)	0.30·10 ⁻⁴	0.833

We incorporated these TiO₂ compact layers into complete MSSCs and present the current-voltage curves in Figure S1. The optimum concentration for performance was 20 mol % TiAcAc, which we use for the remainder of the study. We then varied the thickness of the compact TiO₂ films by varying the TiO₂ sol concentration. We present the photovoltaic performance parameters for devices with the range of compact layer thicknesses in Figure S2, where we found the optimum thickness to be approximately 45 nm.

In Figure 2 we present solar cell current voltage curves and performance parameters comparing the best performing MSSC fabricated with the optimised low temperature processed TiO₂ formulation (lt-TiO₂) as compared to devices employing high temperature processed TiO₂ (ht-TiO₂) and amorphous TiO_x. We show the solar cell performance parameters, along with the solar cell series resistance determined by fitting the slope of the JV curve near open-circuit in Table 2. Devices with the optimum low temperature processed compact layer surpass the performance of previous state-of-the-art sintered compact layer devices, delivering a maximum power conversion efficiency of 15.3%. The improvement is mainly due to higher fill factor, which rises above 0.7 in the best devices, consistent with reduced overall series resistance in the solar cell. Following from this work, we re-optimized the perovskite precursor concentration in the spin-coated solution (see experimental section) and achieved further increase in the film thickness, and overall performance of the solar cells, delivering a maximum full sun power conversion efficiency of 15.9%, with an average of 14.7%. The increased performance arising from an average increase in the short-circuit photocurrent. We present the statistical distribution of the photovoltaic parameters of the optimised batch (ht-TiO₂ vs lt-TiO₂) in Figure S4.



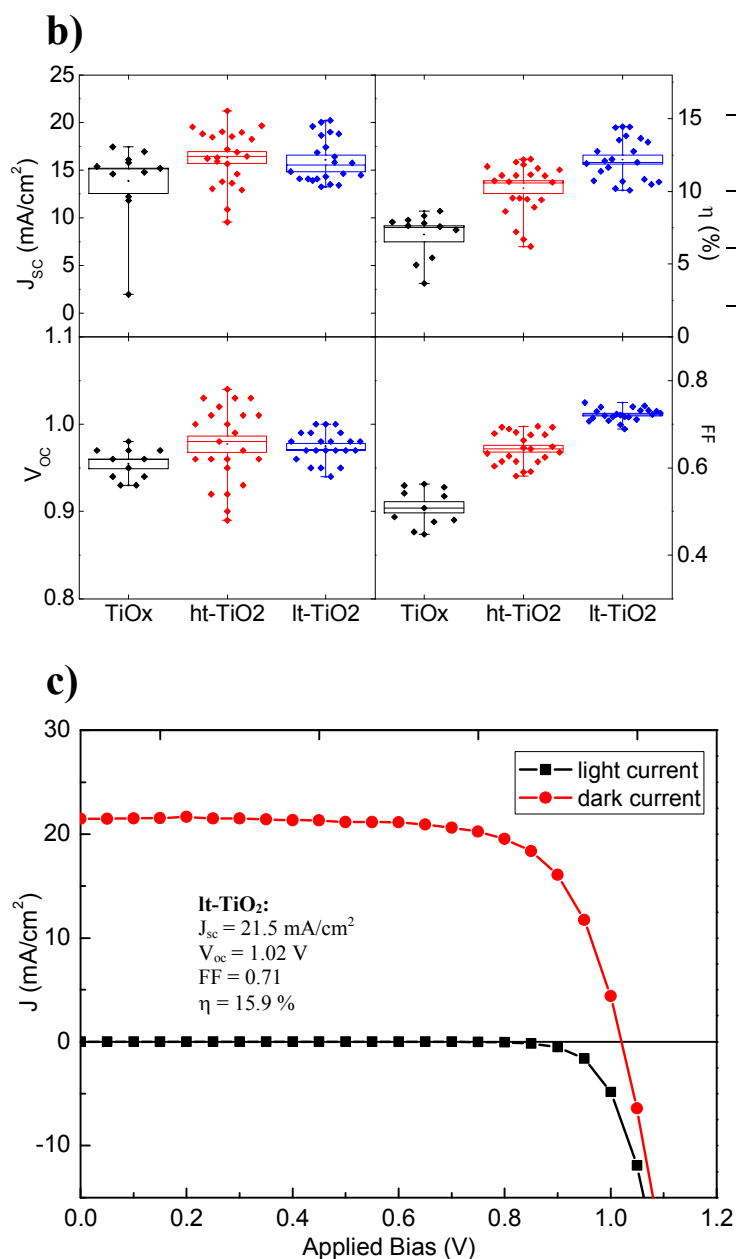


Figure 2. (a) Current-voltage characteristics of the best performing solar cells made with amorphous (TiO_x), high-temperature (ht-TiO₂) and low-temperature (lt-TiO₂) processed compact layer; (b) photovoltaic parameters extracted from current-voltage measurements of a series of solar cells with the different compact layers; (c) record lt-TiO₂ solar cell performance obtained by increasing perovskite film thickness.

Table 2. Photovoltaic parameters extracted from current-voltage measurements of devices with different compact layers.

Compact layer (mean ± s.d.)	J _{sc} (mA cm ⁻²)	η (%)	V _{oc} (V)	FF	R _s (Ω cm ²)
TiO _x	13.85 ± 4.30	7.03 ± 1.59	0.95 ± 0.02	0.51 ± 0.04	18.93 ± 4.87
ht-TiO ₂	16.33 ± 2.98	10.22 ± 1.74	0.98 ± 0.04	0.64 ± 0.04	9.22 ± 1.19
lt-TiO ₂ (20 mol% TiAcAc)	16.06 ± 2.37	12.18 ± 1.46	0.97 ± 0.02	0.72 ± 0.01	6.12 ± 0.88

The new low temperature processed compact TiO₂ is of higher conductivity than the previously sintered material, and the ensuing solar cells have characteristics of lower overall series resistance in the. Fortuitously, this isn't offset by faster recombination (which we show in SI) nor a less favourable band offset, which we infer from the relative invariance in the open-circuit voltage. At first sight the reduced series resistance in the solar cell is surprising, since the ht-TiO₂ should have only been contributing on the order of 0.5 Ω cm² to the solar cell series resistance. In addition, we have previously reasoned for solid-state dye-sensitized solar cells that the series resistance at open-circuit is limited by hole-conduction through spiro-OMeTAD²⁷. However, here the spiro-OMeTAD is simply a solid capping layer (~250 nm thick as opposed to 2 μm infiltrated into a porous medium in the dye-sensitized solar cells) with a conductivity of close to 3 × 10⁻⁵ Scm⁻¹.^{27,28} Hence the overall series resistance expected through a 250 nm thick film of doped spiro-OMeTAD is only 0.8 Ω cm². However, the overall series resistances of the devices are much higher than the sum of bulk resistances of compact layer and hole transporter (see Table 1 and 2), and the difference between the devices incorporating lt-TiO₂ and ht-TiO₂ is over 3 Ω cm². Some of the extra resistance could arise from contact resistance, either present at the perovskite/TiO₂ or the TiO₂/FTO contacts. In particular, there is prior evidence for a potential barrier present at the FTO/TiO₂ interface²⁹⁻³¹. Via Mott-Schottky analysis, the donor density in conventional high temperature processed

compact layers employed in dye-sensitized solar cells is in the order of 10^{19} cm^{-3} .³² Assuming a dielectric of 100 for the TiO_2 , a space charge depletion width, W , can be calculated using,³²

$$W = \sqrt{\frac{2\epsilon\epsilon_0(E-E_{fb})}{eN}} \quad (1)$$

Where N is the concentration of electron donors, ϵ is TiO_2 dielectric constant, ϵ_0 is vacuum permittivity and E_{fb} is the flat-band potential. $E-E_{fb}$ is at approximately the difference between the FTO work function (-4.4 eV)³³ and the fermi-level in the TiO_2 (the latter of which should be higher (deeper) than the conduction band edge of TiO_2 at -4.1 eV)³⁴. With a charge density of 10^{19} cm^{-3} , we estimate a depletion width of approximately 20 nm. This is in the order of the film thickness employed for our optimum compact layers, which implies that band bending appears to be appropriate. However, it also implies that significant depletion throughout the compact layer could occur for the thinnest films, greatly increasing the bulk series resistance beyond that measured from the isolated films on glass. For the low temperature TiO_2 here, the conductivity is between 10 to 100 times greater than both the high temperature films presented here and those fabricated by spray pyrolysis deposition³². If this increase in conductivity is largely due to an increase in the donor density, then with a donor density of 10^{20} , the depletion width would reduce to 6 nm. In this instance the film would not be completely depleted giving much higher bulk conductivity, and additionally the narrower barrier width should enable a lower contact resistance. We note that heavily doping semiconductors at semiconductor-metal contacts is routine to minimise contact resistance³⁵.

To probe the origin of the reduced series of the lt-TiO_2 devices in more detail, we have performed small perturbation transient photovoltage and photocurrent decay measurements, from which we can determine the differential capacitance of the solar cell³⁶. This is usually employed to probe the chemical capacitance of mesoporous

TiO_2 , with the differential capacitance being interpreted to reflect the density of states in the tail of the TiO_2 conduction band. Here, we are using it to probe any changes which may have been introduced due to the different compact TiO_2 layers. In Figure 3 we show that the differential capacitance as a function of open-circuit voltage is considerably different for the devices with the different compact layers. This is quite surprising, since we would assume the chemical capacitance of such a thin film of TiO_2 to be very low. Devices with ht-TiO_2 show much broader distribution of states than cells with lt-TiO_2 , suggesting significant reduction in sub-band gap states in the low temperature processed films, or that the sub bandgap states are predominantly filled in the lt-TiO_2 , consistent with the enhanced conductivity. Alternatively, the capacitance could be due to the depletion of the compact TiO_2 at the FTO interface, which as discussed above, will lead to a considerably broader depletion region in the ht-TiO_2 than the lt-TiO_2 films. In addition, capacitance which may be present due to accumulation or depletion within the perovskite at the perovskite/ TiO_2 interface may also contribute. We note that although these measurements and rational indicates that that a potential barrier at the FTO- TiO_2 interface could be contributing to the series resistance in the solar cell, Further investigations are required to understand in much more detail the electronic structure across the FTO- TiO_2 and TiO_2 -perovskite heterojunctions.

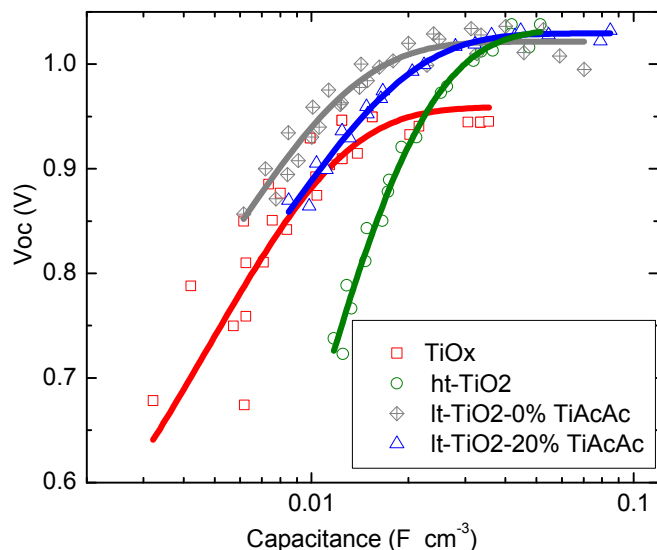


Figure 3. Open circuit voltage against the differential capacitance.

Conclusions

In summary, we have successfully developed a route for creating a low temperature processed TiO₂ compact layer and in doing so we have finally removed all the high temperature thermal processing steps for the mesosuperstructured and planar heterojunction perovskite solar cells. Through this work, we have discovered that the previously employed high temperature processed compact TiO₂ layer, was contributing significantly to the series resistance of the solar cells. The new low temperature approach has hence additionally resulted in improved fill factors and efficiency, pushing the solution processed MSSC back to the very highest efficiencies for perovskite solar cells. This work now makes the MSSC compatible with polymer foil flexible substrates, and opens the door for monolithic multi-junction perovskite solar cells.

3. Experimental

Unless otherwise stated, all materials were purchased from Sigma-Aldrich or Alfa Aesar and used as received. Spiro-OMeTAD was purchased from Borun Chemicals and used as received. The

synthesis of the perovskite, CH₃NH₃PbI_{3-x}Cl_x has been reported elsewhere¹⁰. TiO₂ nanoparticles were synthesized following a previously reported method²². In a typical synthesis 2ml of anhydrous TiCl₄ (99.9%) was added dropwise while stirring into a vial containing 8 ml of anhydrous ethanol. The whole content was transferred into a 100 ml flask containing 40 ml anhydrous benzyl alcohol. The solution was heated to 80 °C and reacted for 9 hours. After that time the reaction was stopped by cooling down the solution, which contained a translucent dispersion of very fine TiO₂ nanoparticles. Then, 4 ml of the above solution was mixed with 36 ml of diethyl ether resulting in the precipitation of the TiO₂. The precipitate was centrifuged, washed in acetone and redispersed in anhydrous ethanol, resulting in a colloidal solution of approximately 28 mg TiO₂/ml ethanol (3.54 wt. % of TiO₂). The formulation was further diluted 3 times (1.18 wt. % of TiO₂) in anhydrous ethanol and the appropriate amount of TiAcAc (10-20 mol % with respect to TiO₂ content) was added directly. The solution was left to stand for at least 2 hours before use, but is stable for months. The low temperature TiO₂ compact layer (lt-TiO₂) was prepared by spin-coating the colloidal dispersion of anatase particles in anhydrous ethanol, formulated with TiAcAc, followed by drying at 150 °C for 30 minutes. The thickness of the compact layer was tuned by the concentration of TiO₂ nanoparticles (3.54 – 0.24 wt. % TiO₂ to ethanol). As standard control samples, blocking layers of non-crystalline TiO_x and high temperature processed TiO₂ (ht-TiO₂) were used. The former was prepared by spin-coating a precursor solution (titanium isopropoxide, TTIP) in anhydrous ethanol (0.254 M) with the addition of a 0.02 M HCl followed by annealing at 150 °C for 30 min, the latter was prepared by spin-coating the same solution (TTIP), followed by annealing at 150 °C and sintering at 500 °C.

Photovoltaic devices were fabricated on fluorine-doped tin oxide (FTO) coated glass (Pilkington, TEC7). Substrates were

ARTICLE

cleaned in hallmanex, then 10 minutes sonication in acetone, 10 minutes sonication in IPA, and 10 minutes of oxygen plasma etching. Compact layers were deposited by spin-coating, as described above. An alumina scaffold was deposited according to the previously reported method which employs Al_2O_3 nanoparticles of 20 nm in diameter¹¹. After depositing the alumina scaffold samples were transferred into a nitrogen-filled glovebox, initially optimised precursor solution of the concentration of 350 mg/ml ($\text{CH}_3\text{NH}_3\text{I}$ and PbCl_2 , 3:1 molar ratio in dimethylformamide (DMF)) was spin-coated at room temperature, followed by annealing at 100 °C for 90 minutes. The concentration of precursor solution was re-optimised to 400 mg/ml, resulting in an increased perovskite film thickness. The hole transporter was deposited by spin-coating an 8 wt. % 2,2',7,7'-tetrakis-(N,N-di-pmethoxyphenylamine)9,9-spirobifluorene (spiro-OMeTAD) in chlorobenzene with added tert-butylpyridine (tBP) and lithium bis(trifluoromethanesulfonyl)imide (Li-TFSI) of 80 and 30 mol %, with respect to spiro-OMeTAD. Finally, 150 nm thick silver electrodes were deposited on top of devices by thermal evaporation at $\sim 10^{-6}$ bar, through a shadow mask.

3.1 Characterization techniques

UV-Vis absorption spectra were obtained using a Carry 300 Bio (Agilent Technologies) spectrometer. Scanning Electron Microscopy images were obtained from Hitachi S-4300 microscope. Conductivity measurements of TiO_2 films were performed by evaporating gold electrodes through the shadow mask on the spin-coated compact layers and using 4-point probe set up with a Keithley 2400 as a sourcemeter. The electrode pattern was designed for 4-point probe measurements with an outer probe channel dimensions of 1 mm (length) x 1 cm (width) and an inner probe separation of 300 μm . The thickness of the channel (TiO_2 layer) was determined from SEM cross-sectional image. X-ray diffraction spectra were

obtained from powder samples (the nanoparticle solution was dried in air at 150 °C) using Panalytical X'Pert Pro X-ray diffractometer.

Current voltage characteristics of solar cells were measured under simulated AM1.5 100 mW cm^{-2} sunlight (ABET Technologies Sun 2000) with a Keithley 2400 sourcemeter. The lamp was calibrated with an NREL-calibrated KG5 filtered silicon reference with a solar mismatch factor of 1.01. The active area of the device was defined by a metal mask with square aperture of the area of 0.0625 cm^2 . The pre-masked active area of the solar cells was approximately 0.12 cm^2 nominally defined by the overlap area of the silver and FTO electrodes. Solar cells were masked for all the current voltage measurements.

Acknowledgements

This work was supported by EPSRC, Oxford Photovoltaics Ltd. and the European Research Council (ERC) through the HYPER PROJECT no. 279881.

Notes and references

* Department of Physics, University of Oxford, Clarendon Laboratory, Parks Road, Oxford OX1 3PU, UK. E-mail: h.snaith1@physics.ox.ac.uk

† Footnotes should appear here. These might include comments relevant to but not central to the matter under discussion, limited experimental and spectral data, and crystallographic data.

Electronic Supplementary Information (ESI) available: additional SEM images, photovoltaic performance parameters and recombination lifetime with a description of photovoltage and photocurrent decay measurements. See DOI: 10.1039/b000000x/

1. C. H. Lee, D. R. Kim, I. S. Cho, N. William, Q. Wang, and X. Zheng, *Scientific reports*, 2012, **2**, 1000.
2. D. J. Lipomi and Z. Bao, *Energy & Environmental Science*, 2011, **4**, 3314.
3. M. B. Schubert and J. H. Werner, *Materials Today*, 2006, **9**, 42–50.

4. A. J. Baca, K. J. Yu, J. Xiao, S. Wang, J. Yoon, J. H. Ryu, D. Stevenson, R. G. Nuzzo, A. a. Rockett, Y. Huang, and J. a. Rogers, *Energy & Environmental Science*, 2010, **3**, 208.
5. M. Kaltenbrunner, M. S. White, E. D. Głowacki, T. Sekitani, T. Someya, N. S. Sariciftci, and S. Bauer, *Nature communications*, 2012, **3**, 770.
6. S. Esiner, H. van Eersel, M. M. Wienk, and R. a. J. Janssen, *Advanced Materials*, 2013, **25**, 2932–2936.
7. M. A. Green, K. Emery, Y. Hishikawa, W. Warta, and E. D. Dunlop, *Progress in Photovoltaics: Research and Applications*, 2013, **21**, 827–837.
8. A. Kojima, K. Teshima, Y. Shirai, and T. Miyasaka, *Journal of the American Chemical Society*, 2009, **131**, 6050–1.
9. H.-S. Kim, C.-R. Lee, J.-H. Im, K.-B. Lee, T. Moehl, A. Marchioro, S.-J. Moon, R. Humphry-Baker, J.-H. Yum, J. E. Moser, M. Grätzel, and N.-G. Park, *Scientific reports*, 2012, **2**, 591.
10. M. M. Lee, J. Teuscher, T. Miyasaka, T. N. Murakami, and J. Henry, *Science*, 2012, **338**, 643–647.
11. J. M. Ball, M. M. Lee, A. Hey, and H. J. Snaith, *Energy & Environmental Science*, 2013, **6**, 1739.
12. J. Burschka, N. Pellet, S.-J. Moon, R. Humphry-Baker, P. Gao, M. K. Nazeeruddin, and M. Grätzel, *Nature*, 2013, **499**, 316–319.
13. M. Liu, M. B. Johnston, and H. J. Snaith, *Nature*, 2013, **501**, 395–398.
14. J.-Y. Jeng, Y.-F. Chiang, M.-H. Lee, S.-R. Peng, T.-F. Guo, P. Chen, and T.-C. Wen, *Advanced Materials*, 2013, **25**, 3727–32.
15. S. Sun, T. Salim, N. Mathews, M. Duchamp, C. Boothroyd, G. Xing, T. C. Sum, and Y. M. Lam, *Energy & Environmental Science*, 2014, DOI: 10.1039/c3ee43161d.
16. P. Docampo, J. M. Ball, M. Darwich, G. E. Eperon, and H. J. Snaith, *Nature communications*, 2013, **4**, 2761.
17. B. Peng, G. Jungmann, C. Jäger, D. Haarer, H.-W. Schmidt, and M. Thelakkat, *Coordination Chemistry Reviews*, 2004, **248**, 1479–1489.
18. C. Y. Jiang, W. L. Koh, M. Y. Leung, S. Y. Chiam, J. S. Wu, and J. Zhang, *Applied Physics Letters*, 2012, **100**, 113901.
19. D. Muñoz-rojas, H. Sun, D. C. Iza, J. Weickert, L. Chen, H. Wang, L. Schmidt-mende, and J. L. Macmanus-driscoll, *Progress in Photovoltaics: Research and Applications*, 2013, **21**, 393–400.
20. J. N. Hart, D. Menzies, Y.-B. Cheng, G. P. Simon, and L. Spiccia, *Journal of Sol-Gel Science and Technology*, 2006, **40**, 45–54.
21. H.-J. Kim, J.-D. Jeon, D. Y. Kim, J.-J. Lee, and S.-Y. Kwak, *Journal of Industrial and Engineering Chemistry*, 2012, **18**, 1807–1812.
22. J. Wang, J. Polleux, J. Lim, and B. Dunn, *Journal of Physical Chemistry C*, 2007, **2**, 14925–14931.
23. L. Kavan, J. Procházka, T. M. Spatler, M. Kalbác, M. Zúkalová, T. Drezen, and M. Graetzel, *Journal of The Electrochemical Society*, 2003, **150**, A1000.
24. E. J. W. Crossland, N. Noel, V. Sivaram, T. Leijtens, J. a. Alexander-Webber, and H. J. Snaith, *Nature*, 2013, **495**, 215–219.
25. J. M. Szeifert, D. Fattakhova-rohlfing, D. Georgiadou, V. Kalousek, J. Rathouský, D. Kuang, S. Wenger, S. M. Zakeeruddin, M. Gra, and T. Bein, *Chemistry of Materials*, 2009, **21**, 1260–1265.
26. H.-J. Chen, L. Wang, and W.-Y. Chiu, *Materials Chemistry and Physics*, 2007, **101**, 12–19.
27. A. Abate, T. Leijtens, S. Pathak, J. Teuscher, R. Avolio, M. E. Errico, J. Kirkpatrick, J. M. Ball, P. Docampo, I. McPherson, and H. J. Snaith, *Physical chemistry chemical physics*: PCCP, 2013, **15**, 2572–9.
28. T. Leijtens, J. Lim, J. Teuscher, T. Park, and H. J. Snaith, *Advanced Materials*, 2013, **25**, 3227–3233.
29. H. J. Snaith and M. Grätzel, *Advanced Materials*, 2006, **18**, 1910–1914.
30. S. Ru and D. Cahen, *The Journal of Physical Chemistry B*, 2004, **108**, 17946–17951.
31. S. Rühle and T. Dittrich, *The Journal of Physical Chemistry B*, 2005, **109**, 9522–9526.
32. L. Kavan and M. Graetzel, *Electrochimica Acta*, 1995, **40**, 643–652.
33. A. Andersson, N. Johansson, P. Bröms, N. Yu, D. Lupo, and W. R. Salaneck, *Advanced Materials*, 1998, **10**, 859–863.
34. M. Grätzel, *Nature*, 2001, **414**, 338–344.
35. A. Y. C. Yu, *Solid-State Electronics*, 1970, **13**, 239–247.

ARTICLE

36. P. Docampo, S. Guldin, M. Stefik, P. Tiwana, M. C. Orilall, S. Hüttner, H. Sai, U. Wiesner, U. Steiner, and H. J. Snaith, *Advanced Functional Materials*, 2010, **20**, 1787–1796.